

X-RAY SPECTROSCOPY OF THE HIGHLY MAGNETIZED PULSAR PSR J1846–0258, ITS WIND NEBULA AND HOSTING SUPERNOVA REMNANT KES 75

E. V. GOTTHELF,¹ S. SAFI-HARB,² S. M. STRAAL,^{3, 4} AND J. D. GELFAND^{3, 4, 5}

¹*Columbia Astrophysics Laboratory, Columbia University, 550 West 120th Street, New York, NY 10027-6601, USA*

²*Department of Physics and Astronomy, University of Manitoba, Winnipeg, MB R3T 2N2, Canada*

³*NYU Abu Dhabi, PO Box 129188, Abu Dhabi, United Arab Emirates*

⁴*Center for Astro, Particle, and Planetary Physics (CAP³), NYU Abu Dhabi, PO Box 129188, Abu Dhabi, United Arab Emirates*

⁵*Center for Cosmology and Particle Physics (CCPP, Affiliate), New York University, 726 Broadway, Room 958, New York, NY 10003*

Submitted to ApJ

ABSTRACT

We present broad-band X-ray spectroscopy of the energetic components that make up the supernova remnant (SNR) Kesteven 75 using concurrent 2017 Aug 17–20 *XMM-Newton* and *NuSTAR* observations, during which the pulsar PSR J1846–0258 is found to be in the quiescent state. The young remnant hosts a bright pulsar wind nebula powered by the highly-energetic ($\dot{E} = 8.1 \times 10^{36}$ erg s^{−1}) isolated, rotation-powered pulsar, with a spin-down age of only $P/2\dot{P} \sim 728$ yr. Its inferred magnetic field ($B_s = 4.9 \times 10^{13}$ G) is the largest known for these objects, and is likely responsible for intervals of flare and burst activity, suggesting a transition between/to a magnetar state. The pulsed emission from PSR J1846–0258 is well-characterized in the 2–50 keV range by a power-law model with photon index $\Gamma_{\text{PSR}} = 1.24 \pm 0.09$ and a 2–10 keV unabsorbed flux of $(2.3 \pm 0.4) \times 10^{-12}$ erg s^{−1} cm^{−2}. We find no evidence for an additional non-thermal component above 10 keV in the current state, as would be typical for a magnetar. Compared to the *Chandra* pulsar spectrum, the intrinsic pulsed fraction is $71 \pm 16\%$ in 2–10 keV band. A power-law spectrum for the PWN yields $\Gamma_{\text{PWN}} = 2.03 \pm 0.02$ in the 1–55 keV band, with no evidence of curvature in this range, and a 2–10 keV unabsorbed flux $(2.13 \pm 0.02) \times 10^{-11}$ erg s^{−1} cm^{−2}. The *NuSTAR* data reveal evidence for a hard X-ray component dominating the SNR spectrum above 10 keV which we attribute to a dust-scattered PWN component. We model the dynamical and radiative evolution of the Kes 75 system to estimate the birth properties of the neutron star, the energetics of its progenitor, and properties of the PWN. This suggests that the progenitor of Kes 75 was originally in a binary system which transferred most its mass to a companion before exploding.

Keywords: ISM: individual (Kes 75) — pulsars: individual (PSR J1846–0258) — stars: neutron

1. INTRODUCTION

To date over 2000 ‘ordinary’ rotation-powered pulsars (RPPs) have been discovered, nearly all as radio pulsars. Their beamed emission is powered by the rotational energy loss from a radiating magnetic dipole of the neutron star (NS) as it gradually slows down (Shapiro & Teukolsky 1983). Young, energetic isolated pulsars often display radio and/or X-ray pulsar wind nebulae (PWN). It is the conversion of rotational energy into electromagnetic radiation and a particle wind that is thought to energize these synchrotron nebulae (Gaensler, & Slane 2006).

Corresponding author: E. V. Gotthelf; eric@astro.columbia.edu

In contrast, magnetars (e.g., Turolla et al. 2015) are also young, isolated NSs but they typically lack the persistent radio emission and the synchrotron nebulae of the rotation-powered pulsars. In their quiescent state, these slowly rotating pulsars (2–12 s) emit uniquely in the X-ray band. Most notably, their thermal X-ray emission far exceeds their rotational kinetic energy loss rate (\dot{E}) and are thought to be powered, instead, by the decay of their enormous magnetic field, above the quantum critical value of $B_{\text{QED}} \equiv m_e^2 c^3 / e\hbar = 4.4 \times 10^{13}$ G (Duncan & Thompson 1992).

Recent exceptions to the defining properties of both the rotation-powered pulsars and the magnetars are shedding new light on their evolution and emission mechanisms: 1) over the last few years, a growing number of “low B-field” magnetars have been detected,

whose magnetic fields border those of the rotation-powered pulsars (e.g., [Rea 2014](#)) 2) the so-called transient magnetars which are seen to display intermittent radio emission during their outbursts (e.g., [Camilo et al. 2008](#)), 3) recent evidence for the first detection of a wind nebula around a magnetar (*Swift* J1834.9–0846; [Younes et al. 2016](#)) and 4) the discovery of variability in a PWN surrounding the rotation-powered, high-B radio pulsar J1119–6127, that has shown a magnetar-like behavior [Blumer \(2017\)](#).

A remarkable new result is the discovery of magnetar-like millisecond bursts from PSR J1846–0258 in Kes 75 ([Gavriil et al. 2008](#); [Kumar & Safi-Harb 2008](#); [Ng et al. 2008](#)). This highly energetic ($\dot{E} = 8.3 \times 10^{36}$ erg s $^{-1}$), 325 ms X-ray rotation-powered pulsar ([Gotthelf et al. 2000](#)), with its bright wind nebula, is located within the core of the young SNR Kes 75 ([Helfand et al. 2003](#); [Su et al. 2009](#); [Temim et al. 2012](#)). The pulsar was caught serendipitously in 2006 in a flaring state, with a notably softening of its spectrum and some PWN morphology change. And most recently, 14 years later, renewed activity is reported from the pulsar ([Kimm et al. 2020](#)). However, the energetics and spectral properties of this pulsar otherwise strongly distinguish it from a magnetar. We might be catching a unique and rare evolutionary state, possibly observing breakout from a buried magnetar-strength magnetic field (see [Halpern & Gotthelf 2010](#)).

We have obtained new, concurrent *XMM-Newton* and *NuSTAR* observations of the Kes 75 system in order to better study the spectral properties of its components, to infer their interactions and evolution. In §2, we describe these data sets, analyzed in conjunction with a recent archival *Chandra* data. We find that a simple power-law model is sufficient to characterize the spectrum of the pulsar, with no evidence for a flatter spectral component above ~ 10 keV, a characteristic of the magnetars. The spectrum of the PWN, also well-modeled by a single power-law, shows no evidence of curvature. We measure a dust scattered halo that manifest as a hard > 10 keV spectral component for the SNR spectrum.

Based on these spectral results, in §3 we apply a dynamical and radiative evolution model to spectral energy distribution (SED) of the Kes 75 system. Finally, in §4, we discuss the implications of our broad-band spectral and evolution modeling. The discovery of magnetar-like activity from the young rotation-powered pulsar offers a unique opportunity to study the connection between distinct nature of rotation-powered pulsars and magnetars, their birth and early evolution.

2. X-RAY OBSERVATIONS AND ANALYSIS

2.1. *NuSTAR*

We observed Kes 75 with *NuSTAR* 2017 Aug 17 as part of the AO3 Guest Observer programs. The nominal 100 ks exposure started at 18:56:09 UT and lasted for

208 ks, with Earth block accounting for periodic orbital time gaps. *NuSTAR* consists of two co-aligned X-ray telescopes, with corresponding focal plane detector modules FPMA and FPMB, each of which is composed of a 2×2 -node CdZnTe sensor array ([Harrison et al. 2013](#)). These are sensitive to X-rays in the 3–79 keV band, with a characteristic spectral resolution of 400 eV FWHM at 10 keV. The multi-nested foil mirrors provide 18" FWHM (58" HPD) imaging resolution over a 12.2' \times 12.2' field-of-view (FoV) ([Harrison et al. 2013](#)). The nominal timing accuracy of *NuSTAR* is ~ 2 ms rms, after correcting for drift of the on-board clock, with the absolute timescale shown to be better than < 3 ms ([Mori et al. 2014](#); [Madsen et al. 2015](#)). This is more than sufficient to resolve the signal from PSR J1846–0258.

NuSTAR data were processed and analyzed using **FTOOLS** 09May2016_V6.19 (**NUSTARDAS** 14Apr16_V1.6.0) with *NuSTAR* Calibration Database (CALDB) files of 2016 July 6. The resulting dataset provides a total of 95 ks of net good exposure time. For all subsequent analysis we merged data from the two FPM detectors. As shown in Figure 1, the small diameter SNR Kes 75 was fully imaged on the FPM detectors, centered on node-0. The pulsar is unresolved from the PWN emission, and its contribution is taking into account in the spectral analysis, using *Chandra* data.

2.2. *XMM-Newton*

We also obtained a shorter, but uninterrupted 51.4 ks *XMM-Newton* observation of Kes 75 on 2017 Aug 19 starting at 14:28:17 UT, overlapping the end of the *NuSTAR* observation, 1.81 days from its start. The European Photon Imaging Camera (EPIC) on-board *XMM-Newton* consists of three detectors, the EPIC pn detector ([Strüder et al. 2001](#)) and EPIC MOS1 and MOS2 ([Turner et al. 2001](#)). These sit at the focal plane of co-aligned multi-nested foil mirrors with an on-axis point spread function with FWHM of $\sim 12.5'$ and $\sim 4.3''$ at 1.5 keV, for the pn and MOS, respectively. The EPIC detectors are sensitive to X-rays in the 0.15–12 keV range with moderate energy resolution of $E/\Delta E(\text{pn}) \sim 20–50$.

The EPIC pn data were obtained in **PrimeSmallWindow** mode ($4.3' \times 4.4'$), with an increased time resolution of 6 ms, sufficient to phase-resolve PSR J1846–0258, at the expense of a large 29% deadtime. The pulsar, PWN, and the main clumps of the SNR are imaged in the FoV (see Fig 1). To resolve possible rapid bursts from the pulsar we operated EPIC MOS2 in **FastUncompressed** mode, which offers 1.5 ms time resolution with 1D-imaging on the central EPIC CCD, at the expense of an increase in the background component. The MOS1 data were acquired in $1.8' \times 1.8'$ **PrimePartialW2** small-window mode on the central CCD with the PWN just filling the reduced FoV. The time resolution in this mode is 300 ms, useful for searching for slower flares but insufficient to resolved PSR J1846–0258.

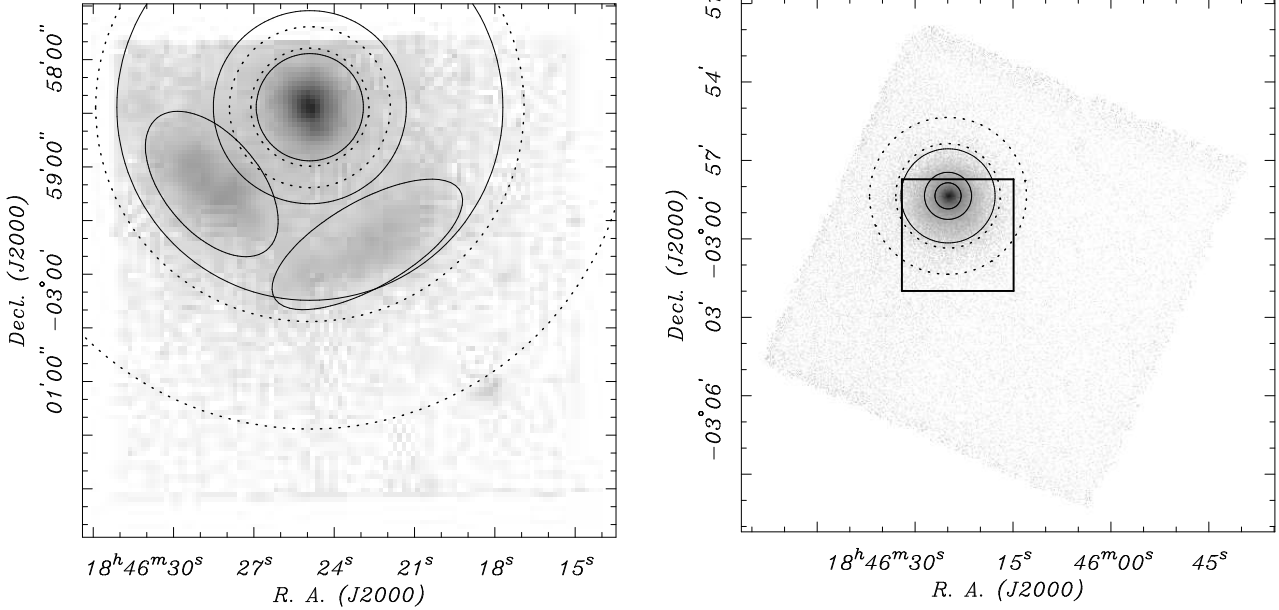


Figure 1. Low resolution X-ray images of Kes 75 scaled logarithmically to highlight faint emission. Shown are the spectral extraction regions for the source (solid circles) and background (dotted circles) as described in the text. Left — The *XMM-Newton* EPIC pn small window mode image in the 1–10 keV band. The SNR emission is highly cut off below 1 keV. Right — The *NuSTAR* 3–79 keV image. The pulsar and PWN are unresolved and overlap the much fainter SNR emission in this band. The EPIC pn field of view is overlaid on the *NuSTAR* image (solid box).

Data were reduced and analyzed using the Standard Analysis Software (SAS) v.15 with the most up-to-date calibration files. After filtering out background flares we obtained usable live time of 50.1/36.1 ks, for the MOS/pn data.

2.3. Archival *Chandra* data

To correct and verify our *XMM-Newton* analysis of Kes 75, we used archival *Chandra* data to spatially resolve in the same band-pass the pulsar, PWN, and SNR components and obtain the most accurate fluxes. Of the many *Chandra* observations of Kes 75 obtained over the years, we select for this work ObsID #18030, a deep observation acquired closest in time to our concurrent *XMM-Newton* and *NuSTAR* data set. This observation was carried out with the Advanced CCD Imaging Spectrometer (ACIS) on 2016 June 8 with an exposure time of 86 ks. The data were reprocessed and cleaned using standard CIAO v4.10 routines, resulting in an effective exposure time of 84.9 ks. The *Chandra* count rate from PSR J1846–0258 relative to the 3.14 s nominal ACIS CCD frametime results in a $\sim 6\%$ pile-up fraction for the pulsar. This produces evident distortion in its spectrum that is mitigated by including the *Chandra* pileup model in all spectral fits with ACIS of the pulsar presented herein. We compare our joint fits results to those obtained using data from earlier epochs (Helfand et al. 2003; Morton et al. 2007; Kumar & Safi-Harb 2008; Ng et al. 2009; Su et al. 2009; Temim et al. 2012) as presented in Table 1.

2.4. Timing Analysis

In the following timing analysis, all photon arrival times are converted to barycentric dynamical time (TDB) using the DE405 solar system ephemeris and the *Chandra* coordinates given in Helfand et al. (2003). We extracted photons using an aperture of radius $r < 0'.75$ and $r < 1.3'$ for the *XMM-Newton* and *NuSTAR* data, respectively, found to maximize the embedded pulse signal. For *NuSTAR*, we include photons over the full energy band and but restricted our analysis to the 0.5–10 keV band for the *XMM-Newton* data to minimize particle contamination.

We searched for the known signal from PSR J1846–0258 using an accelerated FFT to account for the substantial frequency derivative associated with the pulsar. Photon arrival times from the long(er) *NuSTAR* data were binned into a 0.01 s light curve and searched at the full resolution allowed by the span of the data. A highly significant signal is recovered near the expected frequency and its derivative. We refine the strongest signal using the Z_1^2 test (Buccheri et al. 1983), appropriate for the nearly sinusoidal pulse profile (see Figure 2). In the following phase-resolved spectroscopy, we use the best-fit period $P = 0.32852377(4)$ s and period derivative $\dot{P} = 7.4(4) \times 10^{-12}$ for epoch MJD 58013.

We also searched from PSR J1846–0258 for possible millisecond bursts similar to those detected by *RXTE* (Gavriil et al. 2008), we examined its light curves over a range of timescales down to the 10 ms. We compared

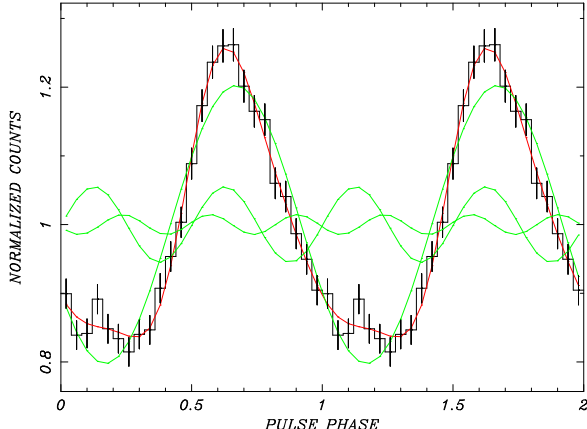


Figure 2. The background subtracted pulsed profiles of PSR J1846–0258 using data obtained from the *NuSTAR* observation presented here. Overplotted on the data is a model profile (red) composed of the sum of the first three Fourier components (green) for the light curve. This profile, for the full energy band, is normalized to the average counts per bin.

the frequency of occurrence of counts in each light curve bin to those predicted by Poisson statistics based on the mean count rate and find no significant outliers. We therefore conclude that, during the duration of our *NuSTAR*/*XMM-Newton* observation, the pulsar did not display significant temporal characteristics of a magnetar.

2.5. Spectral Analysis

For spectral fitting we use the `XSPEC` (12.10.0c) package (Arnaud 1996) and characterize the column density with the built-in `TBabs` absorption model, selecting the `wilm` Solar abundances (Wilms et al. 2000) and the `vern` photoionization cross-section (Verner et al. 1996). The χ^2 statistic is used to evaluate the spectral fits throughout and the parameter uncertainties are quoted at the 90% confidence level (C.L.) for one or more interesting parameters, as appropriate. Response matrices and ancillary response files were generated for each data set following the mission specific standard procedures. We note that previous spectral fits in the literature used the `Wabs` absorption model, a photoelectric absorption using the Wisconsin cross-sections (Morrison & McCammon 1983). Spectral fits using the newer column density model can result in a measured value that is significantly different, for the same intrinsic spectrum model.

2.5.1. PSR J1846–0258 Pulsed Spectrum

To isolate the broad-band pulsed component of PSR J1846–0258 in the *XMM-Newton* and *NuSTAR* spectra, we divided the pulse profile into two phase intervals, corresponding to the peak (“on” pulse) and the valley (“off” pulse) regions. Although the valley spectrum provides a perfect representation of the unpulsed background to subtracted from the peak spectrum, it

necessarily includes a portion of the pulsed emission itself. For a theoretical sinusoidal signal, the flux correction factor for the background subtracted pulsed spectrum is $\pi/2 = 1.57$. In our case, where the pulse profile is more peaked than a sine curve, the computed correction factors are 1.41 and 1.30 in the 2–10 keV band, for the *XMM-Newton* and *NuSTAR* data, respectively. This assumes that the pulse shape is essentially energy independent, for which there is no significant evidence to the contrary.

We choose source apertures of $r < 30''$ radius to extract the pulsar spectra for each mission to help estimate the total flux from the pulsar and to generate point-source response matrices. As the source (“on”) and background (“off”) spectra contain a similar number of counts per channel, their subtraction results in large uncertainties. With this in mind, we group all source spectra into spectral fitting channels that contain a minimum signal-to-noise of 3 sigma after background subtraction.

The joint *XMM-Newton* and *NuSTAR* pulsed spectrum is well-fit to a simple absorbed power-law model in the 2–10 keV and 3–50 keV range, respectively. The column density is poorly constrained in these fits and is fixed to $N_{\text{H}} = 6 \times 10^{22} \text{ cm}^{-2}$, the iterated value obtained from the final, high statistic PWN analysis (described below). The best-fit photon index is $\Gamma = 1.24 \pm 0.09$, with a $\chi^2_{\nu} = 0.992$ for 36 DoF. The corrected 2–10 keV unabsorbed flux is $F_x = 2.16^{+0.25}_{-0.26} \times 10^{-12} \text{ erg s}^{-1} \text{ cm}^{-2}$ and $F_x = 2.42^{+0.29}_{-0.18} \times 10^{-12} \text{ erg s}^{-1} \text{ cm}^{-2}$ for the *XMM-Newton* and *NuSTAR* spectral fits, respectively. These fluxes are self-consistent within the measurement uncertainties. We note, moreover, that the mean pulsed flux of $F_x = (2.25 \pm 0.35) \times 10^{-12} \text{ erg s}^{-1} \text{ cm}^{-2}$, is fully consistent with the 2–10 keV flux predicted by the curved power-law model of Kuiper (2018), $F_x = 2.35 \times 10^{-12} \text{ erg s}^{-1} \text{ cm}^{-2}$, used to characterize the X-ray to gamma-ray flux.

To estimate the pulsed fraction for PSR J1846–0258, we extracted a total pulsar spectrum from the 2016 *Chandra* observation using a $1.5''$ aperture and an $2'' < r < 3''$ annular background region. A fit to an absorbed power-law in the 1–10 keV range with the column density fixed at $N_{\text{H}} = 4.0$ yields a best-fit $\Gamma = 1.32 \pm 0.15$, with a $\chi^2_{\nu} = 1.19$ for 66 DoF. The total pulsar unabsorbed flux is $F = (3.1 \pm 0.1) \times 10^{-12} \text{ erg s}^{-1} \text{ cm}^{-2}$, implying an intrinsic pulsed fraction of $71 \pm 16\%$ in 2–10 keV band, assuming that the pulsar flux has been steady between the two observations, which is evidently the case, as shown in the next section.

To compare our pulsed measurements to published results on PSR J1846–0258 obtained at earlier epochs we re-fitting these spectra using the historic `XSPEC` `Wabs` model for the interstellar absorption Helfand et al. (2003); Kumar & Safi-Harb (2008); Ng et al. (2008). These results are summarized in Table 1.

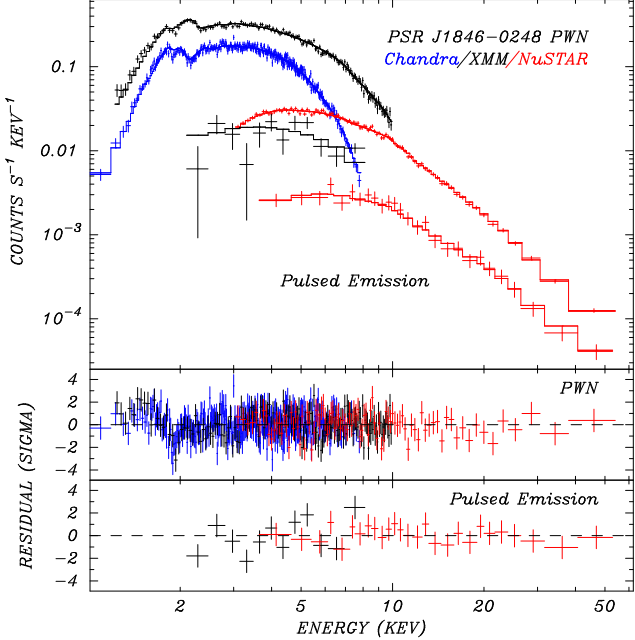


Figure 3. Broad-band X-ray spectra of PSR J1846–0258 and its PWN in SNR Kes 75. The *Chandra* (blue), and concurrent *XMM-Newton* EPIC pn (black) and *NuSTAR* (red) Kes 75 PWN spectra are fitted jointly (top three curves). Similarly for the *XMM-Newton* EPIC pn and *NuSTAR* phase-resolved pulsed spectra (lower two curves). Both sets of spectra are fitted to an absorbed power-law model with independent normalizations. For the PWN spectra, the *XMM-Newton* model included a component to account for the pulsar emission below ~ 2 keV and the *NuSTAR* spectrum includes a component for the pulsed emission, significant > 30 keV (see text for details). Upper Panel — the data points (*crosses*) are plotted along with the best fit model (*histogram*) given in Table 2. Lower panels — the best fit residuals for PWN (upper) and pulsed emission (lower) spectra in units of sigma.

2.5.2. PSR J1846–0258 PWN Spectrum

As noted above, it is not possible to spatially isolate the PWN from the pulsar emission in the *XMM-Newton* and *NuSTAR* data sets. Instead, we fit the composite spectrum and account for the pulsar emission in the source aperture with an additional power-law component. For *XMM-Newton*, we estimate the pulsar contribution using the spatial resolved *Chandra* results, and for *NuSTAR*, we use the measured pulsed spectrum, both presented above. This is necessary to account for significant contaminated below ~ 2 keV in the *XMM-Newton* PWN spectrum from the pulsar and its environment, and for the pulsed emission that distorts the *NuSTAR* spectrum above ~ 30 keV. For the *XMM-Newton* spectra we use a $r < 30''$ source aperture that captures most of the PWN flux and averages over its radial-dependence spectrum. For the *NuSTAR*

Table 1. Spectra of PSR J1846–0258 in Kes 75

Reference	N_H (10^{22} cm $^{-2}$)	Γ	Flux ^a [$\times 10^{-12}$]
<i>Chandra</i> 2000 data set			
Helfand et al. 2003	3.96 (fixed)	1.39 ± 0.04	7.1
Ng et al. 2008	4.0 (fixed)	1.1 ± 0.01	6.1 ± 0.03
Gavriil et al. 2008	...	$1.17_{-0.12}^{+0.15}$...
Kumar et al. 2008	3.96 (fixed)	$1.32_{-0.09}^{+0.08}$	4.3 ± 0.2
<i>Chandra</i> 2006 data set (Flare Epoch)			
Ng et al. 2008	4.0 (fixed)	1.86 ± 0.02	37 ± 01.0
Gavriil et al. 2008	...	$1.89_{-0.06}^{+0.04}$...
Kumar et al. 2008	$4.15_{-0.12}^{+0.09}$	$1.97_{-0.07}^{+0.05}$	27_{-2}^{+1}
<i>Chandra</i> 2016 data set			
This Work	4.0 (fixed)	1.32 ± 0.15	3.1 ± 0.1
<i>XMM-Newton</i> & <i>NuSTAR</i> 2017 data sets (Pulsed Only)			
This Work	4.0 (fixed)	1.23 ± 0.09	2.2 ± 0.4

Column density is derived using the built-in `XSPEC Wabs` interstellar absorption model in all cases for comparison purpose. Quoted uncertainties for 90% C.L. for one interesting parameter.

^aUnabsorbed 2–10 keV flux, in units of erg cm $^{-2}$ s $^{-1}$.

spectrum, with its poorer spatial resolution, we use a smaller $r < 24''$ source aperture, to account for the additional blur of the PWN flux in order to better match the *XMM-Newton* spectrum extraction region, while simultaneously minimizing possible contamination from the nearby SNR lobes. For both missions, we estimate the SNR background in the source aperture using a concentric annular background region $33'' < r < 45''$. We note that background contribution is small (<10%) except below ~ 2 keV. As the PWN is poorly resolved spatially in both telescopes, we again use point-source mirror response matrices to characterize the effective area.

The spatially averaged *XMM-Newton* and *NuSTAR* PWN spectra are fitted jointly with their normalization left free to allow for systematic differences in the aperture flux. The spectrum is well-modelled by an absorbed power-law over the 1.2–50 keV span of the two data sets. This yields a column density $N_H = (6.0 \pm 0.1) \times 10^{22}$ cm $^{-2}$ and photon index $\Gamma = 2.03 \pm 0.02$, with a $\chi^2_{\nu} = 1.04$ for 399 degrees-of-freedom (DoF). We

note that, without taking into account the pulsar component in these spectra it is not possible to get a consistent power-law index in the overlapping 3–10 keV band. To check for evidence of spectral curvature we fitted a broken power-law model to the joint spectrum, however, no significant change in the index is measurable in the current data.

We next compare the 2016 *Chandra* PWN spectrum to the above *XMM-Newton* result, over their mutual energy range. A spectra was extracted from the $r < 30''$ *XMM-Newton* region, excluding a $r < 2''$ circle around the pulsar. The best fit power-law model in the 1.0–8 keV band yields $N_H = (5.9 \pm 0.2) \times 10^{22} \text{ cm}^{-2}$ and photon index $\Gamma = 2.00 \pm 0.06$, with a $\chi^2_\nu = 1.07$ for 306 DoF. These parameters are consistent with the *XMM-Newton* results, suggesting no spectral change between the two epochs, and if so, the *Chandra* flux is considered the most accurate. It is reassuring that the details of the residuals of both spectra are effectively identical. The common systematic deviations in the spectra suggest that they are related to differences in the SNR emission between the source and background regions.

Finally, to obtain the most accurate PWN spectrum and flux measurement, we re-fitted the joint *XMM-Newton* and *NuSTAR* PWN spectra with the addition of the *Chandra* spectrum, again with independent normalizations. The best-fit parameters are $N_H = (6.0 \pm 0.1) \times 10^{22} \text{ cm}^{-2}$ and photon index $\Gamma = 2.0 \pm 0.02$, with a $\chi^2_\nu = 1.075$ for 548 DoF. The final 2–10 keV unabsorbed PWN flux of $(2.13 \pm 0.03) \times 10^{-11} \text{ erg s}^{-1} \text{ cm}^{-2}$, is determined from the *Chandra* component of this fit, after allowing for the missing flux from the excluded pulsar region, a $\sim 10\%$ effect. This missing flux is estimated from a spectrum of the bright northern PWN knot, extracted from a $r < 2''$ aperture. The ratio of the pulsar to the total flux (pulsar+PWN) is consistent with the observed pulsed fraction $\sim 10\%$ in the 2–10 keV band. The pulsar and PWN spectral results are reported in Table 2

2.5.3. Kes 75 SNR Spectrum

We also extracted *XMM-Newton* and *NuSTAR* spectra for the SNR emission using an $0.9' < r < 1.8'$ source annulus and $2' < r < 3'$ background region (see Figure 1). This covers the two bright X-ray clumps labeled southeast (SE) clump and southwest (SW) clump in [Helfand et al. \(2003\)](#), encompassing the bulk of the remnant emission. For *XMM-Newton*, in small window mode, the SNR fell partially off the field of view but still includes the clumps.

The spectra of the SNR were fitted to a non-equilibrium thermal plasma model (`XSPEC NEI`) with variable abundances plus a power-law component (see Table 3), as indicated in the first *Chandra* study by [Helfand et al. \(2003\)](#). This model produces an excellent fit, but with parameter values notably different from those reported in the earlier *Chandra* studies (e.g.,

Table 2. Spectra of the pulsar and PWN in Kes 75

Parameter	Pulsar		PWN
	Pulsed	Total	
$N_H (10^{22} \text{ cm}^{-2})$	6.0 (fixed)	6.0(fixed)	6.0 ± 0.1
Photon Index Γ	1.24 ± 0.09	1.38 ± 0.16	2.03 ± 0.02
$F[\times 10^{-11}]^a$ (abs.)	0.18 ± 0.03	0.24 ± 0.01	1.53 ± 0.02
$F[\times 10^{-11}]^b$ (unabs.)	0.23 ± 0.04	0.31 ± 0.01	2.13 ± 0.02
Luminosity L_x^c	9.9×10^{33}	1.3×10^{34}	9.2×10^{34}
$\chi^2_\nu (DoF)$	0.99(36)	1.19(66)	1.04(399)

Note — Quoted uncertainties for 90% C.L. for one or two interesting parameters, for the pulsar and PWN, respectively. Pulsed emission is from the a joint *XMM-Newton/NuSTAR* phase-resolved spectroscopy; the total pulsar flux is determined from a fit to the *Chandra* data (see text for details)

^aAbsorbed 2–10 keV flux, in $\text{erg cm}^{-2} \text{ s}^{-1}$.

^bUnabsorbed 2–10 keV flux, in erg s^{-1} .

^c2–10 luminosity, in erg s^{-1} , for $d = 6 \text{ kpc}$.

[Helfand et al. 2003](#); [Temim et al. 2012](#)). This can be attributed, at least in part, to the updated ISM model used herein and to the difference in the extraction regions.

We next included the *Chandra* data described in §2.3 to the joint *XMM-Newton* and *NuSTAR* fit, to verify *XMM-Newton* spectrum in their common energy range and for an improved flux measurement. We find that that: a) a single component (`XSPEC NEI`) with variable abundances does model the data well, confirming the need for an additional harder component; b) both a two-temperature NEI model and an NEI+power-law model provide an improved fit to the spectra. However, the *XMM-Newton*'s greater sensitivity to the hard diffuse X-ray emission, along with the expanded *NuSTAR* energy band allowed us to clearly select the power-law model as prefer over the thermal NEI model. The best fit model parameters obtained with the joint fit are presented in Table 3.

As noted above, the plasma temperature of the NEI model (softer component) differs because of the chosen `TBabs` with the `wilm` abundances. Previous works used the [Anders & Grevesse \(1989\)](#) abundances accounting for the lower column density and lower temperatures. We confirm this by checking against the results obtained using the early *Chandra* observation (`Obsid 748`), re-processes with the latest calibrations.

The background for each spectrum is generally less than an order of magnitude of the source flux, up to about 20 keV, beyond which it dominates the *NuSTAR* spectrum. Small systematic errors in the power-law index are possible due to different in the size of the PSF

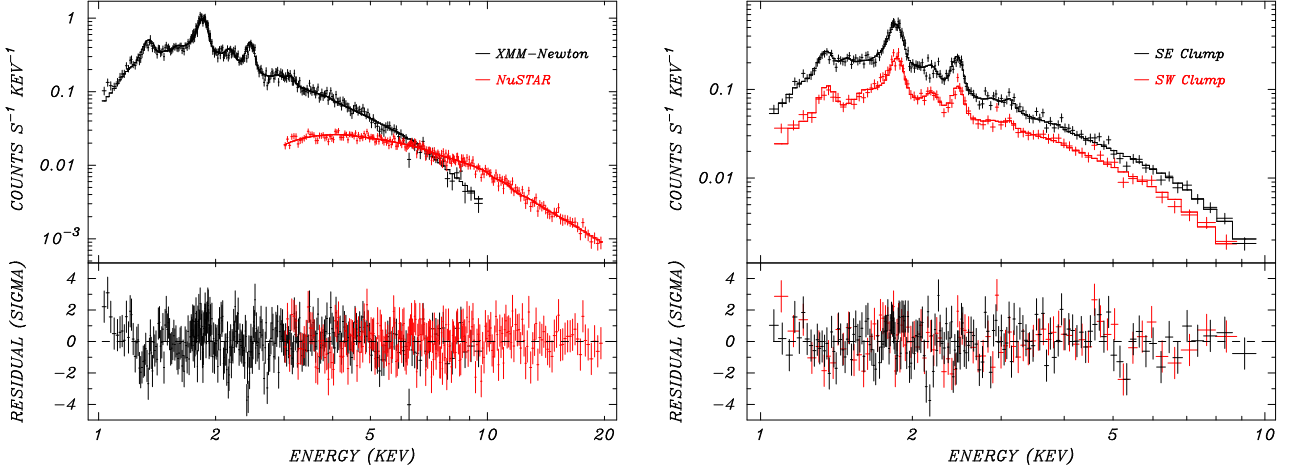


Figure 4. The spectrum of Kes 75 fitted to an absorbed non-equilibrium thermal plasma (NEI) plus power-law model. Right — Joint fit to the concurrent *XMM-Newton* EPIC pn (black) and *NuSTAR* (red) spectra with independent normalizations. The EPIC pn data that covers the bulk of the bright sector, as described in the text. Left — The *XMM-Newton* EPIC pn X-ray spectrum of the bright thermal emission from the southeast clump (black) and the southwest clump (red). Upper Panels — data points (crosses) plotted along with the best fit models (histogram) are given in Table 3. Lower panels — the best fit residuals in units of sigma.

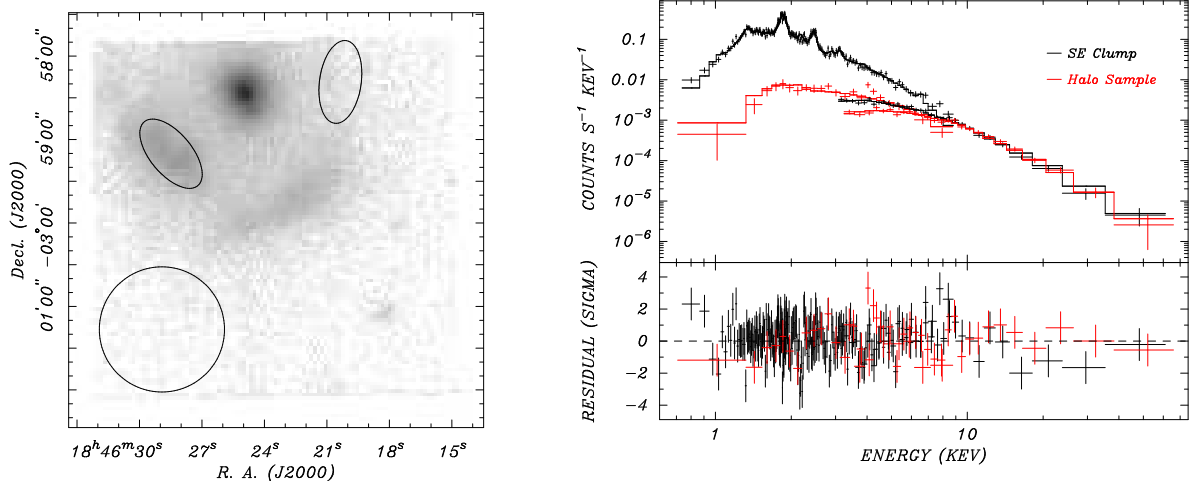


Figure 5. Evidence of a dust scattered PWN halo component in hard SNR spectra of Kes 75. Left — An *XMM-Newton* image of the Kes 75 SNR showing the location of mirrored source regions, situated on opposite sides of the SNR, one centered on the SE clump (left) and the other placed to sample the halo region (right), equi-distant from the pulsar. The large circle shows the background region. Right — A joint fit to the concurrent *XMM-Newton* and *NuSTAR* spectra extracted from the two regions fitted with the NEI plus power-law model with their power-law indices linked. There is no evidence for excess thermal emission in the halo region and the flux from this region is sufficient to account for the hard continuum component in the SE Clump spectrum.

for the two missions over the source aperture. However, this is likely to be a small effect because emission from outside the source aperture still contributes proportionally more by area to offset the losses from the larger surface brightness emission inside the aperture.

Using the *XMM-Newton* data alone, we also analysed the two clump regions separately. Because of its larger PSF, the clumps are not well isolated in the *NuSTAR* data, and we do not attempt a joint spectral fit

with the *XMM-Newton* data. The clump extraction regions and results are presented in Table 3. An annular ($2.2' < r < 3.0'$) background region, centered at coordinates $18:46:24.862 - 02:58:28.312$ (J2000), is used for both clumps.

We have also attempted a two-temperature component fit as done in previous studies (e.g. Temim et al. 2012). We find that the spectra require temperatures of ~ 0.9 keV and 4.6 keV for the cool and hotter

Table 3. Spatially resolved spectra of SNR Kes 75

	Southeast	Southwest	Sector ^a
Region R.A.	18:46:22.764	18:46:28.574	18:46:24.893
Region Decl.	-02:59:43.33	-02:59:09.53	-02:58:28.31
Ellipse radii	1'0 × 0'4	0'8 × 0'45	...
Ellipse P.A.	300°	40°	...
Annulus radii	0'9 × 1'8
N_{H} (10 ²² cm ⁻²)	4.11 ^{+0.11} _{-0.10}	4.27 ^{+0.23} _{-0.31}	4.14 ^{+0.11} _{-0.09}
kT (keV)	1.01 ^{+0.17} _{-0.10}	1.18 ^{+0.24} _{-0.20}	0.87 ^{+0.05} _{-0.06}
τ (10 ¹⁰ s cm ⁻³)	8.5	4.2	10.0 ^{+2.2} _{-1.6}
Mg	0.89 ^{+0.09} _{-0.11}	0.76 ^{+0.20} _{-0.16}	0.81 ± 0.08
Si	1.26 ^{+0.15} _{-0.13}	1.21 ^{+0.46} _{-0.28}	1.27 ± 0.09
S	0.98 ^{+0.17} _{-0.14}	1.0 ^{+0.53} _{-0.27}	1.15 ± 0.11
NEI Flux (10 ⁻¹¹) ^b	3.2	1.7	10
Photon Index Γ	1.73 ^{+0.33} _{-0.63}	2.02 ^{+0.37} _{-0.92}	2.02 ^{+0.04} _{-0.05}
PL Flux (10 ⁻¹²) ^b	1.6	1.3	8.7
χ^2_{ν} (DoF)	1.459 (452)	1.369 (363)	1.369 (896)

See Figure 1 for the SNR clump regions. Coordinates are in the J2000 system. Quoted uncertainties for 90% C.L. for the parameter of interest.

^a Joint fit to *XMM-Newton* EPIC pn, *Chandra* and *NuSTAR* spectra, with independent normalizations.

^b Unabsorbed *XMM-Newton* EPIC pn flux measured in the 0.5–10 keV band in units of erg s⁻¹ cm⁻². The first two columns correspond to the clumps fits using the *XMM-Newton* and *Chandra* dataset.

component, respectively, of the southeast clump, and ~ 0.85 keV and 3.2 keV for southwest clump. However, the reduced chi-squared in the 2T-component fits is higher (≥ 1.5) than for the thermal+power-law model, and the *vnei* ionization timescale is too low in the 2T-component fits. We therefore again favor the power-law interpretation of the hard component. This result is consistent with the joint fit of the SNR sector with the *NuSTAR* data. Below, and in §4.2, we discuss the nature of the hard component and link it to a dust scattered PWN halo.

2.6. Evidence for a Dust Scattered PWN Halo

The need for a highly significant hard continuum component to model the SNR spectra of Kes 75 has been evident since the first spatially resolved X-ray observations reported by Helfand et al. (2003), and later by Su et al. (2008); Temim et al. (2012). These authors considered several possible origins for this non-thermal emission and concluded that a dust scattered PWN halo is the most consistent with the data. Furthermore, by comparing *Chandra* observations taken during and post flare epochs, Reynolds et al. (2018) found spatial evidence for

a "transient halo", likely depended on the brightness of the pulsar/PWN.

To better understand this hard component we compare broad-band spectra of the SNR's SE clump with that obtained from a mirrored region on the other side of the SNR, that lacks evidence of thermal emission, to represent the putative halo emission. For the SE SNR clump we extracted spectra from a 15'' × 30'' region, smaller then used in Section 2.5.3, to minimize the background contribution to the source region. As shown in Figure 5, the halo and the SE clump regions are equidistant from the pulsar; a background region is chosen well away from the SNR, to allow for the instrumental signature and the local Galactic ridge emission.

Figure 5 presents the joint fit to the *XMM-Newton* and *NuSTAR* spectra using the NEI plus power-law model, with the photon indices for the clump and the halo spectra linked; the thermal component is set to zero for the halo fits. The *NuSTAR* data is crucial to isolate the higher-energy component in a band where it is most dominant. As expected, this fit to the SE clump spectrum reproduced that reported in Table 3. Notably, the best-fit model yields a power-law index of $\Gamma = 1.97 \pm 0.09$, consistent with that found for the PWN spectrum. The averaged 2–10 keV surface brightness in the halo aperture $\sim 1'2$ away from the pulsar is 6.0×10^{29} erg/s/arcsec² at 6 kpc. Most importantly, the flux from the clump and the halo spectrum in the *NuSTAR* band is essentially the same (see Figure 5).

These results suggest that most, if not all, of the hard emission component for the SNR clumps can be attributed to a non-localized spectral component. To consider the radial dependence of this component, we examined a *Chandra* spectrum obtained from the 33'' $< r < 45''$ annular region between the PWN and the clumps. This region is found to be an add-mixture of the thermal component and the power-law emission, with a similarly hard photon index (~ 2), and a surface brightness that is approximately a factor of 3 times larger than that of the western halo region. The decrease in surface brightness of the hard component away from the pulsar is consistent with a dust-scattered PWN halo interpretation, as further discussed in section 4.

3. PWN-SNR MODELING

Currently, the best way of determining the energetics of the Kes 75 progenitor, the birth parameters of PSR J1846–0258, and for its pulsar wind, is to fit the observed properties of the PWN with a model for its dynamical and radiative evolution (see Gelfand 2017 for a recent review of such models). Following our previous analysis of Kes 75 (Gelfand et al. 2014) and similar SNR/PWN systems (e.g., G54.1+0.3, Gelfand et al. 2015; HESS J1640–465, Gotthelf et al. 2014), we use a Markoff Chain Monte Carlo code to determine the combination of input parameters of such a model (based on that described by Gelfand et al. 2009) best reproduce

(lowest χ^2) the observed properties of Kes 75 listed in Table 4. The input parameters are listed in Table 5, with the age t_{age} and initial spin-down luminosity \dot{E}_0 chosen that, for a given braking index p and spin-down timescale τ_{sd} , reproduce the pulsar's current characteristic age t_{ch} and spin-down luminosity \dot{E} :

$$t_{\text{age}} = \frac{2t_{\text{ch}}}{p-1} - \tau_{\text{sd}} \quad (1)$$

$$\dot{E}_0 = \dot{E} \left(1 + \frac{t_{\text{age}}}{\tau_{\text{sd}}} \right)^{\frac{p+1}{p-1}}, \quad (2)$$

the PWN's inverse Compton emission is the result of leptons scattering of the Cosmic Microwave Background and an additional photon field with temperature T_{ic} and normalization K_{ic} , defined such that the energy density u_{ic} of this photon field is:

$$u_{\text{ic}} = K_{\text{ic}} a_{\text{bb}} T_{\text{ic}}^4, \quad (3)$$

where $a_{\text{bb}} = 7.5657 \times 10^{-15} \frac{\text{erg}}{\text{cm}^3 \text{K}^4}$, as well as assuming the spectrum of particle injected into the PWN at the termination is well described by a broken power-law:

$$\frac{d\dot{N}_{e^\pm}}{dE}(E) = \begin{cases} \dot{N}_{\text{break}} \left(\frac{E}{E_{\text{break}}} \right)^{-p_1} E_{\text{min}} < E < E_{\text{break}} \\ \dot{N}_{\text{break}} \left(\frac{E}{E_{\text{break}}} \right)^{-p_2} E_{\text{break}} < E < E_{\text{max}} \end{cases} \quad (4)$$

$$(5)$$

where \dot{N}_{e^\pm} is the rate e^\pm are injected into the PWN and \dot{N}_{break} is calculated requiring that at all times:

$$(1 - \eta_B) \dot{E} \equiv \int_{E_{\text{min}}}^{E_{\text{max}}} E \frac{d\dot{N}_{e^\pm}}{dE} dE, \quad (6)$$

where the magnetization of the wind η_B is defined to be the fraction of the pulsar's spin-down luminosity injected into the PWN as magnetic fields. Unfortunately, the number of model parameters is one more than the number of observed quantities for this system, and the set of input parameters which produced the lowest χ^2 ($\chi^2 = 0.93$) are provided in Table 5 with the observed and predicted spectral energy distribution (SED) of this source shown in Figure 6. The significance and limitations of these results are discussed below.

4. DISCUSSION AND CONCLUSIONS

Based on the 2016 *Chandra* and 2017 *XMM-Newton* and *NuSTAR* observations of PSR J1846–0258 reported herein, the pulsar had returned to its quiescent rotation-powered state following the last known, 2006, magnetar-like event. In this state, we show that there is no evidence in the pulsed emission for an additional, flatter spectral component above 10 keV, as reported for many magnetars (den Hartog e.g., 2008; see reviews by

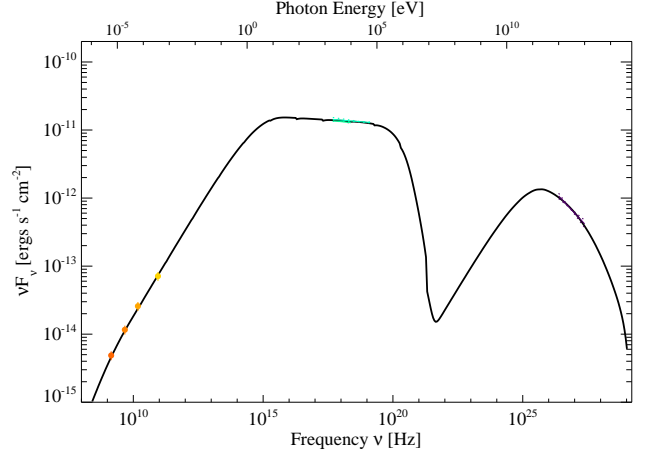


Figure 6. Observed (color) and predicted (black line) spectral energy distribution (SED) of the PWN in Kes 75. The observed and predicted quantities are provided in Table 4, while the model parameters are shown in Table 5.

Mereghetti et al. 2015; Kaspi et al. 2017). The pulsar is found to be highly modulated in the 2–10 keV band with a lower limit of at least 64%, not atypical for young X-ray pulsars with sinusoidal pulse profiles. The new, high quality spectral measurements confirms the relation between the power-law slopes for PSR J1846–0258 and its PWN, consistent with that predicted for other highly energetic rotation-powered pulsars (Gotthelf 2003). The flux from the PWN is consistent with that reported by Reynolds et al. (2018) and we find no evidence of curvature in its broad-band 1–55 keV spectrum.

The efficiency of powering the PWN from spin-down radiative losses, ($L_x/\dot{E} \approx 1\%$), estimated from the 2–10 keV luminosity at distance of 6 kpc (Leahy & Tian 2007; Kumar & Safi-Harb 2008), is among the highest known for rotation-powered pulsars. The discovery of magnetar activity suggest that at least part of the pulsar luminosity could be from surface emission from the pulsar, however, the spectrum of the pulsar in the quiescent state, quite distinct from that expected from a magnetar, typically characterize by a hot, 0.5 keV blackbody emission and a steep non-thermal component $\Gamma \sim 4$ (Parmar et al. 1998; Marsden & White 2001). It is possible that some of the flux, consistent with the pulsed fraction, could be due to a cooling NS, heated during the magnetar activity. Unpulsed, soft blackbody emission they could be responsible for the lower column density measured for the pulsar relative to that of the PWN, $N_{\text{H}} \sim 4 \times 10^{22} \text{ cm}^{-2}$ and $\sim 6 \times 10^{22} \text{ cm}^{-2}$, respectively. However, the high column density and instrument bandpass limits our ability to investigate this further.

The broad-band X-ray spectroscopy of Kes 75 SNR reveals for the first time that the hard continuum component is dominant above 10 keV, and is clearly independent of the thermal emission. Similar non-thermal

Table 4. Observed and Predicted PWN-SNR Model for Kes 75

Property	Observed	Model	Reference
SNR			
Radius (')	1.5 ± 0.15	1.50	...
Distance (kpc)	$5.8^{+0.5}_{-0.4}$	5.8	Verbiest et al. 2012
PWN			
Radius ('')	30 ± 1.67	30.0	...
$\dot{\theta}_{\text{pwn}}$ (%/yr)	0.249 ± 0.023	0.234	Reynolds et al. 2018
$S_{1.4}$ (mJy)	348 ± 52	327	Salter et al. 1989
$S_{4.7}$ (mJy)	247 ± 37	240	Salter et al. 1989
S_{15} (mJy)	172 ± 26	158	Salter et al. 1989
S_{89} (mJy)	80 ± 12	82	Bock & Gaensler 2005
$\Gamma(2-55 \text{ keV})$	2.031 ± 0.025	2.030	...
$F(2-10 \text{ keV})^a$	2.13 ± 0.022	2.133	...
$\Gamma(1-10 \text{ TeV})$	2.41 ± 0.01	2.42	HESS Collab. 2018
$F(1-10 \text{ TeV})^a$	0.160 ± 0.016	0.159	HESS Collab. 2018
PSR			
\dot{E} (erg s $^{-1}$)	8.10×10^{36}	...	Livingstone et al. 2011
t_{ch} (yr)	728	...	Livingstone et al. 2011
p	2.65 ± 0.01	2.652	Livingstone et al. 2011

Notes — The predicted values are for the set of model parameters which resulted in the lowest χ^2 . Quantities derived in this paper have ... for their reference.

^aFlux in units of 10^{-11} erg cm $^{-2}$ s $^{-1}$

^bwww.atnf.csiro.au/research/pulsar/psrcat (Manchester et al. 2005)

components has been detected from several SNR shells, as first discovered in the specially-resolved spectroscopy of SN 1006 (Koyama et al. 1995). This emission is typically described in the X-ray band by a power-law with a steeper photon index $\sim 2.5-3$ (Reynolds 2008) and can result in particle acceleration up to TeV energies (e.g., Reynolds 2011).

For Kes 75, the flatter spectrum and radial fall-off of the hard emission supports a dust scattering halo origin for this component, that can be attributed to the bright and heavily absorbed pulsar/PWN (Helfand et al. 2003; Su et al. 2009; Temim et al. 2012). Similar halos have been discovered around magnetars or highly magnetized neutron stars that display a magnetar-like outburst (e.g., Esposito et al. 2013; Safi-Harb 2013). In the case of Kes 75, a brightning of the halo was noted follow-

Table 5. Best fit PWN-SNR Model Parameters for Kes 75

Model Parameter	Min. χ^2 Value
Supernova Explosion Energy E_{sn}	1.26×10^{50} erg
Supernova Ejecta Mass M_{ej}	0.51 M_{\odot}
ISM density n_{ism}	0.56 cm^{-3}
Pulsar braking index p	2.652
Pulsar spin-down timescale τ_{sd}	398 yr
Age t_{age}	483 yr
Initial Spin-down Luminosity \dot{E}_0	$4.69 \times 10^{37} \frac{\text{erg}}{\text{s}}$
Pulsar Wind Magnetization η_{B}	0.0724
Min. energy of injected particles E_{min}	2.00 GeV
Break energy of injected particles E_{break}	2042 GeV
Max. energy of injected particles E_{max}	1.00 PeV
Low-energy index of injected particles p_1	1.73
High-energy index of injected particles p_2	3.04
Temperature of IC photon field T_{ic}	32 K
Normalization of IC photon field K_{ic}	1.17×10^{-3}

Notes — Parameters of the model for the evolution of a PWN inside a SNR used to reproduced the observed properties of Kes 75 (Table 4), as well as the values for the combination of parameters which give the lowest χ^2 .

ing the 2006 flare (Reynolds et al. 2018). The current work shows that the halo emission is detectable even during the quiescent state of the pulsar. Such a halo has been also seen from G21.5–0.9, a similarly young, bright and heavily absorbed PWN (e.g., Matheson & Safi-Harb 2010; Bocchino et al. 2005).

Making use of the new X-ray results for Kes 75, we re-evaluated the evolution of the PWN in the SNR using the dynamical and radiative model described in Section 3. The lack of degree of freedoms for this model makes it difficult to draw statistically meaningful results from the fitting, however, the preferred parameters provide insight into the origin and underlying physics in this system. The results of our modeling strongly prefers Kes 75 as originated in a low energy ($E_{\text{sn}} \ll 10^{51}$ ergs), low ejecta mass ($M_{\text{ej}} < 1 \text{ M}_{\odot}$) explosion. These quantities are determined in part by the observed high expansion rate of the PWN (Table 4), which, as discussed by Reynolds et al. (2018), implies the PWN is expanding into low density supernova ejecta. One possibility, as mentioned by Reynolds et al. (2018), is the PWN is currently embedded in a low density bubble resulting from the decay of ^{56}Ni in the innermost ejecta (Li et al. 1993; Chevalier 2005). However, our modeling also simultaneously reproduces the observed size of the PWN and SNR, which is less dependent on the local conditions around the nebula.

Taken at face value, the low values of E_{sn} and M_{ej} have strong implications for its progenitor. The value of M_{ej} is lower than what would be expected for an isolated massive star progenitor (e.g., Sukhbold et al. 2016; Raithel et al. 2018), even when considering substantial mass-loss before exploding as a core-collapse supernova (e.g., Dessart et al. 2011). However, these values are comparable to what was found in recent three-dimensional simulations of neutrino-driven core collapse supernovae of He cores (Müller et al. 2019) – suggesting that the progenitor of Kes 75 was originally in a binary system which transferred most its mass to a companion before exploding, indicative of a high initial mass.

The evolutionary model prefers a low temperature for the IC photon field of $T = 32$ K. This is in agreement with recent findings of dust emitting at a temperature of $T = 33 \pm 5$ K (for silicate grains) by Temim et al. (2019), which they conclude is most likely dust formed by the supernova and being shock heated by the PWN.

Furthermore, since the initial spin period P_0 of a pulsar can be calculated using (e.g., Pacini, & Salvati 1973; Gaensler, & Slane 2006; Slane 2017):

$$P_0 = P \left(1 + \frac{t_{\text{age}}}{\tau_{\text{sd}}} \right)^{-\frac{1}{p-1}}, \quad (7)$$

the similarity between the inferred spin-down timescale τ_{sd} and t_{age} from this modeling suggests that $P_0 \approx 0.618P \approx 200$ ms (e.g., Gotthelf et al. 2000; Livingstone et al. 2011). This is considerably longer than $P_0 \approx 2$ ms needed to explain is strong, spin-down inferred dipole surface magnetic field strength $B_{\text{ns}} \approx 5 \times 10^{13}$ G if it results from an $\alpha - \Omega$ dynamo in the proto-neutron star (e.g., Thompson & Duncan 1993) – as often assumed for this and similar neutron stars (e.g., Granot et al. 2017). However, the high mass for the progenitor inferred above is consistent with the notion that such stars produce strongly magnetized neutron stars (e.g., Gaensler et al. 2005).

Lastly, the properties of the pulsar wind are somewhat atypical for this class of sources. The magnetization $\eta_B \sim 0.07$ inferred from this modeling is $\gtrsim 2 \times$ higher than that inferred from previous analyses of this system ($\eta_B \sim 0.005$; Bucciantini et al. 2011, $\eta_B \sim 0.008 - 0.03$; Torres et al. 2014), though this could be the result of a limited exploration of parameter space and reproducing a different set of observed properties than previous work. Of particular interest is the value of

E_{max} . Current theories suggest that $E_{\text{max},\Phi} \approx e\Phi$ (e.g., Bucciantini et al. 2011), where e is the charge of the electron and Φ is the voltage near the pulsar’s polar cap (e.g., Goldreich, & Julian 1969; Bucciantini et al. 2011; Slane 2017):

$$\Phi = \sqrt{\frac{\dot{E}_{\text{psr}}}{c}} \approx 1.66 \times 10^{13} \text{ statvolt} \times \frac{299.79 \text{ Volt}}{1 \text{ statvolt}} \quad (8)$$

$$\approx 4.99 \times 10^{15} \text{ V,}$$

or $E_{\text{max},\Phi} \approx 5$ PeV. While this value isn’t particularly well-constrained by our modeling, mainly due to the lack of information concerning the MeV emission from this PWN, our results suggest E_{max} agrees with Bucciantini et al. (2011).

In summary, the presented X-ray observations offer a new window to study a unique pulsar-SNR system that represents a transitional object between the rotation-powered pulsars and the magnetars. Continued observations during its outburst and quiescent phases will help to address questions related to its origin and what distinguishes PSR J1846–0258 from the typical pulsar in two classes of neutron stars.

This research was funded by the National Aeronautics and Space Administration (NASA) *NuSTAR* grant 80NSSC17K0636. SSH acknowledges support from the Natural Sciences and Engineering Research Council of Canada (NSERC) and the Canadian Space Agency. The contributions of JDG and SMS was supported by NASA grant NNX17AL74G issued through the NNH16ZDA001N Astrophysics Data Analysis Program (ADAP). The *NuSTAR* mission is a project led by the California Institute of Technology, managed by the Jet Propulsion Laboratory, and funded by NASA. This research made use of the *NuSTAR* Data Analysis Software (NUSTARDAS) jointly developed by the ASI Science Data Center (ASDC, Italy) and the California Institute of Technology (USA). This research also made use of data and software provided by the High Energy Astrophysics Science Archive Research Center (HEASARC), which is a service of the Astrophysics Science Division at NASA/GSFC and the High Energy Astrophysics Division of the Smithsonian Astrophysical Observatory. We also acknowledge use of the NASA Astrophysics Data Service (ADS).

REFERENCES

Anders, E. & Grevesse, N. 1989, *Geochimica et Cosmochimica Acta*, 53, 197

Arnaud, K. A. 1996, in *ASP Conf. Ser.* 101, Astronomical Data Analysis Software and Systems V, ed. G. H. Jacoby & J. Barnes (San Francisco, CA: ASP), 17

Blumer, H., Safi-Harb, S., McLaughlin, M. A. 2017 *ApJ*, 850, L18

Bocchino, F., van der Swaluw, E., Chevalier, R., Bandiera, R. 2005, *A&A*, 442, 539

Bock, D. C.-J., & Gaensler, B. M. 2005, *ApJ*, 626, 343

Buccieri, R., et al. 1983, *A&A*, 128, 245

Bucciantini, N., Arons, J., & Amato, E. 2011, *MNRAS*, 410, 381

Camilo, F., Reynolds, J., Johnston, S., Halpern, J. P., & Ransom, S. M. 2008, *ApJ*, 679, 681

Chevalier, R. A. 2005, *ApJ*, 619, 839

Dessart, L., Hillier, D. J., Livne, E., et al. 2011, *MNRAS*, 414, 2985

den Hartog, P. R., Kuiper, L., Hermsen, W. 2008, *A&A*, 489, 263

Duncan, R. C., Thompson, C. 1992, *ApJ*, 392, L9

Esposito, P., et al. 2013, *MNRAS*, 429, 3123

Gaensler, B. M., McClure-Griffiths, N. M., Oey, M. S., et al. 2005, *ApJL*, 620, L95

Gaensler, B. M., & Slane, P. O. 2006, *ARA&A*, 44, 17

Gavriil, F. P., Gonzalez, M. E., Gotthelf, E. V., Kaspi, V. M., Livingstone, M. A., & Woods, P. M. 2008, *Science*, 319, 1802

Gelfand, J. D., Slane, P. O., & Zhang, W. 2009, *ApJ*, 703, 2051

Gelfand, J. D., Slane, P. O., & Temim, T. 2014, *Astronomische Nachrichten*, 335, 318

Gelfand, J. D., Slane, P. O., & Temim, T. 2015, *ApJ*, 807, 30

Gelfand, J. D. 2017, Modelling Pulsar Wind Nebulae, 161

Goldreich, P., & Julian, W. H. 1969, *ApJ*, 157, 869

Gotthelf, E. V., Vasisht, G., Boylan-Kolchin, M., & Torii, K. 2000, *ApJ*, 542, L37

Gotthelf, E. V. 2003, *ApJ*, 591, 361

Gotthelf, E. V., Tomsick, J. A., Halpern, J. P., et al. 2014, *ApJ*, 788, 155

Granot, J., Gill, R., Younes, G., et al. 2017, *MNRAS*, 464, 4895

Halpern, J. P., Gotthelf, E. V., Reynolds, J., Ransom, S. M. & Camilo, F. 2008, *ApJ*, 676, 1178

Halpern, J. P., & Gotthelf, E. V. 2010, *ApJ*, 709, 436

Harrison, F. A., Craig, W. W., Christensen, F. E. et al. 2013, *ApJ*, 770, 103

Helfand, D. J., Collins, B. F., Gotthelf, E. V. 2003, *ApJ*, 582, 783

H. E. S. S. Collaboration, Abdalla, H., Abramowski, A., et al. 2018, *A&A*, 612, A1

Kaspi, V. M. & Beloborodov, A. M. 2017, *ARA&A*, 55, 261

Krimm, H. A., Lien, A. Y., Page, K. L., Palmer, D. M. & Tohuvavohu, A. 2020, *GCN Cir.* 28187

Koyama, K., Petre, R., Gotthelf, E. V., Hwang, U., Matsuura, M., Ozaki, M., Holt, S. S. 1995, *Nature*, 378, 255

Kumar, H. S. & Safi-Harb, S. 2008, *ApJ*, 678, L43

Leahy, D. A., Tian, W. W. 2007, *A&A*, 461, 1013

Li, H., McCray, R., & Sunyaev, R. A. 1993, *ApJ*, 419, 824

Livingstone, M. A., Ng, C.-Y., Kaspi, V. M., et al. 2011, *ApJ*, 730, 66

Manchester, R. N., Hobbs, G. B., Teoh, A. & Hobbs, M. 2005, *Astron. J.*, 129, 1993

Marsden, D., White, N. E. 2001 *ApJ*, 551, L155

Madsen, K. K., Harrison, F. A., Markwardt, C. B., et al. 2015, *ApJS*, 220, 8

Matheson, H. & Safi-Harb, S. 2010 *ApJ*, 724, 572

Mattana, F., et al. 2009, *ApJ*, 694, 12

Mereghetti, S., Pons, J. A., Melatos, A. 2015, *SSRv*, 191, 315

Mori, K., Gotthelf, E. V., Dufour, F., et al. 2014, *ApJ*, 793, 88

Morrison, R. & McCammon, D. 1983, *ApJ*, 270, 119

Morton, T. D., Slane, P., Borkowski, K. J., Reynolds, S. P., Helfand, D. J., Gaensler, B. M., Hughes, J. P. 2007, *ApJ*, 667, 219

Müller, B., Tauris, T. M., Heger, A., et al. 2019, *MNRAS*, 484, 3307

Ng, C. -Y., Slane, P. O., Gaensler, B. M., Hughes, J. P. 2008, *ApJ*, 686, 508

Ng, C. -Y., Gaensler, B. M., Murray, S. S., Slane, P. O., Park, S., Staveley-Smith, L., Manchester, R. N., Burrows, D. N. 2009, *ApJ*, 706, L100

Pacini, F., & Salvati, M. 1973, *Astrophys. Lett.*, 13, 103

Parmar, A. N., Oosterbroek, T., Favata, F., et al. 1998, *Astron. Astrophys.*, 330, 175

Raihel, C. A., Sukhbold, T., & Özel, F. 2018, *ApJ*, 856, 35

Rea, N. 2014, *IAU*, 302, 429

Reynolds, S. P. 2008, *Annual Rev. Astron. Astrophys.*, 46, 89

Reynolds, S. P. 2011, *Astrophysics and Space Science*, 336, 257

Reynolds, S. P., Borkowski, K. J., & Gwynne, P. H. 2018, *ApJ*, 856, 133

Safi-Harb, S., 2013, *IAUS*, 291, 251

Salter, C. J., Reynolds, S. P., Hogg, D. E., et al. 1989, *ApJ*, 338, 171

Shapiro, S. L. & Teukolsky, S. A. *Black Holes, White Dwarfs, and Neutron Stars: The Physics of Compact Objects* (Wiley, New York, 1983).

Slane, P. 2017, *Handbook of Supernovae*, 2159

Strüder, L. et al. 2001, *A&A*, 365, 18

Su, K. Y. L., Rieke, G. H., Stapelfeldt, K. R., Smith, P. S., Bryden, G., Chen, C. H., Trilling, D. E. 2008 *ApJ*, 679, 125

Su, Y., Chen, Y., Yang, J., Koo, B.-C., Zhou, X., Jeong, I.-G., Zhang, C.-G. 2009 *ApJ*, 694, 376

Sukhbold, T., Ertl, T., Woosley, S. E., et al. 2016, *ApJ*, 821, 38

Thompson, C., & Duncan, R. C. 1993, *ApJ*, 408, 194

Temim, T., Slane, P., Arendt, R. G., Dwek, E. 2012, *ApJ*, 745, 46

Temim, T., Slane, P., Sukhbold, T., Koo, B.-C., Raymond, J. C., Gelfand, J. D. 2019, *ApJ*, 878, L9

Torres, D. F., Cillis, A., Martín, J., et al. 2014, *Journal of High Energy Astrophysics*, 1, 31

Turolla, R., Zane, S., Watts, A. L. 2015, *RPPh*, 78, 690

Turner, M. J. L. 2001, *A&A*, 365, 27

Verbiest, J. P. W., Weisberg, J. M., Chael, A. A., et al. 2012, *ApJ*, 755, 39

Verner, D. A., Ferland, G. J., Korista, K. T., Yakovlev, D. G. 1996, *ApJ*, 465, 487

Wilms, J., Allen, A., & McCray, R. 2000, *ApJ*, 542, 914

Younes, G., Kouveliotou, C., Kargaltsev, O., Gill, R., Granot, J., Watts, A. L., Gelfand, J., Baring, M. G., Harding, A., Pavlov, G. G., van der Horst, A. J., Huppenkothen, D., Göğüş, E., Lin, L., Roberts, O. J. 2016 *ApJ*, 824, 138